RSC Advances

PAPER

View Article Online
View Journal | View Issue

Cite this: *RSC Adv.*, 2020, **10**, 39080

NH_2-MIL-88B ($Fe_\alpha In_{1-\alpha}$) mixed-MOFs designed for enhancing photocatalytic Cr(VI) reduction and tetracycline elimination†

Chunhua Xu,*[a] Mingjun Bao,[b] Jiawen Ren[b] and Zhiguang Zhang *[b]

Aiming at solving the issue of wastewater purification, this work synthesized NH_2-MIL-88B ($Fe_\alpha In_{1-\alpha}$) photocatalysts by a simple one-pot method, which was employed for photocatalytic reduction of Cr(VI) and oxidation of TC-HCl. Compared with traditional NH_2-MIL-88B (Fe) photocatalysts, NH_2-MIL-88B ($Fe_{0.6}In_{0.4}$) displayed excellent photocatalytic performance; the photocatalytic redox rate for Cr(VI) and TC-HCl reached 86.83% and 72.05%, respectively. The good photocatalytic performance might be attributed to the metal-to-metal charge transition (MMCT) between Fe–O clusters and In–O clusters formed by doping In(III) into NH_2-MIL-88B (Fe), which provides effective active sites for the photocatalytic reduction and oxidation routes. Besides, the synergistic effect of the ligand-to-metal charge transition (LMCT) and MMCT expands the separation and transfer of photogenerated carriers and inhibits the recombination of electron–hole pairs, thus effectively improving the photocatalytic performance. Therefore, this work could provide a new method for the construction of mixed metal MOFs for the photocatalytic degradation of pollutants.

Received 31st August 2020
Accepted 18th October 2020

DOI: 10.1039/d0ra07487j

rsc.li/rsc-advances

Introduction

Heavy metals and residual antibiotics in wastewater have become a serious threat to living creatures and the environment.[1–4] Hexavalent chromium (Cr(VI)), as a heavy metal ion pollutant in wastewater with high toxicity and mobility, has seriously threatened human health and the natural environment.[5,6] If a large amount of Cr(VI) existed in the drinking water system, it would cause damage to the human stomach, kidneys, liver, and retinas and also serious environmental concern.[7,8] Therefore, it is urgent to remove Cr(VI) from wastewater. There are many existing solutions such as chemical precipitation,[9] membrane separation,[10] ion exchange,[11] activated carbon adsorption[12] and photocatalytic reduction.[13–15] Among them, the reduction of Cr(VI) to Cr(III) by semiconductor photocatalysis is a very effective strategy due to the low toxicity of Cr(III).[16–18] Furthermore, tetracycline hydrochloride (TC-HCl), as one of the most common antibiotics, is widely used in various industries such as medicine, agriculture, and animal husbandry. TC-HCl is abundant in the environment due to its stable chemical structure and non-biodegradation, which has already imperiled the ecosystem and human health.[19–21] There are many current ways to remove TC-HCl, including adsorption,[22] advanced oxidation processes (AOPs),[21] biological degradation,[23] electrolysis,[24] membrane filtration,[25] ion exchange[26] and photocatalytic degradation.[27,28] Photocatalytic degradation is widely used in recent years because of mild reaction conditions, high efficiency, low cost and greenly.[20,29–31]

Metal–organic frameworks (MOFs), as a class of crystalline inorganic–organic hybrid materials, are composed of the interconnection between metal centers and multidentate organic ligands.[32,33] MOFs have been valued by researchers in the field of photocatalysis[34,35] due to the inherent large specific surface area, uniform and adjustable pore structure, and abundant active sites.[36] Under the irradiation of incident light, the photogenerated electrons are excited from the valence band (VB) and transferred to the conduction band (CB) through the ligand-to-metal charge transition (LMCT) process. The separated photogenerated electrons–holes pairs can perform the reduction and oxidation reaction with the reactants adsorbed on the catalyst surface.[37] Traditional MOFs existed some shortcomings, such as small photoresponse range and high electrons–holes recombination rate.[38] It is undoubtedly a good way to change the photoresponse range and photocatalytic performance of MOFs by adjusting the central metal or organic ligands.[39] The strategy of combining two or more transition metals into the same framework to form mixed-metal MOFs has aroused the interest of researchers.[40]

Mixed-metal organic framework (MM-MOFs), containing two or more metal centers, are periodically arranged with a single ligand in the whole framework.[41,42] There is a metal-to-metal

[a]*Dalian Vocational & Technical College (Dalian Radio and TV University), Dalian 116035, PR China. E-mail: xuchunhua0331@163.com; Tel: +86 411-62614316*
[b]*School of Chemistry and Chemical Engineering, Liaoning Normal University, Dalian 116029, PR China. E-mail: zgzhang@lnnu.edu.cn; Tel: +86 411-82158309*

† Electronic supplementary information (ESI) available. See DOI: 10.1039/d0ra07487j

charge transition (MMCT) process between multiple metals in MM-MOFs, which facilitates the transfer of photogenerated electrons and inhibits the recombination of electrons–holes pairs. Compared with single-metal MOFs, the synergistic effects between LMCT and MMCT of MM-MOFs can effectively improve the photocatalytic activity in various applications.[43] Also, MM-MOFs can effectively control the electronic structure and bandgap structure while increasing the metal active sites.[44–46] For instance, Vu *et al.* synthesized Fe-Cr-MIL-101 for dye degradation by the hydrothermal method. Mixed-metal MOFs showed better adsorption capacity and higher photocatalytic activity and stability in comparison with Cr-MIL-101.[47] Maite P. *et al.* studied the synthesis of multimetal MOFs doped with Zn(II), Ru(III) and Pd(II) into Cu-MOF and applied to electrochemical reduction of CO_2.[48] In our previous report, we successfully synthesized NH_2-MIL-68 ($In_\alpha Fe_{1-\alpha}$) that displayed good photocatalytic activity.[49] According to reports, NH_2-MIL-88B (Fe) has a flexible pore structure and a large open structure channel due to its 3D porous structure containing hexagonal channels and bipyramidal cages.[50] The wide and flexible pore structure facilitated other metal ions to smoothly enter the 3D structure to replace the original central metal ions, and can provide adjustment space for structural changes that may be caused by the introduction of other central metal ions, thereby improving related performance.

Based on the above analysis, a novel MM-MOFs material NH_2-MIL-88B ($Fe_\alpha In_{1-\alpha}$) was constructed and synthesized *via* the one-pot method directly, which used NH_2-MIL-88B (Fe) as the structural framework. Under visible light irradiation, the activity of photocatalytic treatment of pollutants in water was tested. The results showed that the efficiency of Cr(VI) reduction and TC-HCl oxidation of NH_2-MIL-88B ($Fe_\alpha In_{1-\alpha}$) was 1.7 and 1.6 times that of NH_2-MIL-88B (Fe). Moreover, a possible photocatalytic mechanism was proposed through characterization and performance and active species testing. This work provides an effective way for the construction of MM-MOFs and the photocatalytic degradation of various pollutants in wastewater.

Experimental sections

The chemicals and characterization details could be found in ESI.†

Synthesis of NH_2-MIL-88B (Fe)

The NH_2-MIL-88B (Fe) sample was prepared *via* a one-pot method. 2-Aminoterephthalic acid (NH_2-BDC) (0.54 mmol) and $Fe(NO_3)_3 \cdot 9H_2O$ (0.48 mmol) were dissolved in DMF (12 mL), added CH_3CN (12 mL) after mixed well. Then, and the mixture was transferred into a flask, oil bath at 120 °C for 45 min. The suspension was cooled to room temperature naturally and washed with methanol. The sample was dried at 70 °C for 5 h, then NH_2-MIL-88B (Fe) was gained.

Synthesis of In-doped NH_2-MIL-88B (Fe)

In-doped NH_2-MIL-88B (Fe) was synthesized through the above similar process, except that pure $Fe(NO_3)_3 \cdot 9H_2O$ was replaced with different ratios $Fe(NO_3)_3 \cdot 9H_2O$ and $In(NO_3)_3 \cdot xH_2O$. The products were named as NH_2-MIL-88B ($Fe_\alpha In_{1-\alpha}$), and the synthesis diagram was shown in Scheme 1.

Evaluation of photocatalytic performance

The photocatalytic performance of as-obtained samples was evaluated by removing Cr(VI) and TC-HCl. A certain amount of synthesized NH_2-MIL-88B ($Fe_\alpha In_{1-\alpha}$) was added into the Cr(VI) solution and stirring sufficiently. Simultaneously, the pH value of the Cr(VI) solution was adjusted to 2 with HCl solution. Then proceed to photocatalytic degradation. During the experiment, pay attention to the concentration of Cr(VI) in the system. The suspension was stirred for some time under dark conditions. When the concentration of Cr(VI) no longer changed, switch to Xe lamp irradiation. The suspensions taken out regularly are centrifuged and filtered with a 0.22 μm syringe filter. The determination of Cr(VI) was realized by the DPC method with a UV-visible spectrophotometer. The photocatalytic oxidation of TC-HCl is similar to the above process. Where the pH value of the TC-HCl solution was adjusted to 9 with NaOH solution and the determination was realized by the UV-visible spectrophotometer method. The removal adsorption reduction/oxidation efficiency of pollutant is calculated using Lambert Beer's law and the following formula:

$$\text{Efficiency } (\%) = C/C_0 \times 100\% \quad (1)$$

here C and C_0 are the concentrations of pollutants in the water at t and t_0.

Results and discussions

Structure and morphology analysis

As revealed in Fig. 1a, the crystalline structure of NH_2-MIL-88B (Fe) and In-doped NH_2-MIL-88B ($Fe_\alpha In_{1-\alpha}$) are confirmed by the XRD pattern. The obvious characteristic peaks of NH_2-MIL-88B (Fe) located at 9.21°, 10.25°, 13.07°, 16.65°, 18.53°, 20.69°, consistent with the literature reported,[15] verified the successful preparation of NH_2-MIL-88 (Fe). The doped amounts of In on NH_2-MIL-88B (Fe) determined by the ICP-AES analysis as shown in Table S1.† Concomitantly, the main characteristic peaks of NH_2-MIL-88B ($Fe_\alpha In_{1-\alpha}$) appeared in the same position as NH_2-MIL-88B, which preliminarily proved that NH_2-MIL-88B ($Fe_\alpha In_{1-\alpha}$) was successfully prepared. The as-prepared MM-MOFs mainly exist combination and crystal lattice in the form

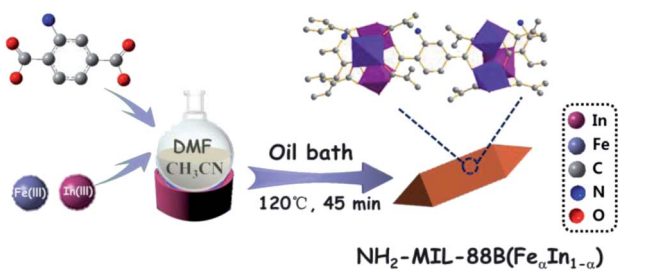

Scheme 1 Synthesis diagram of the synthetic processes of NH_2-MIL-88B ($Fe_\alpha In_{1-\alpha}$).

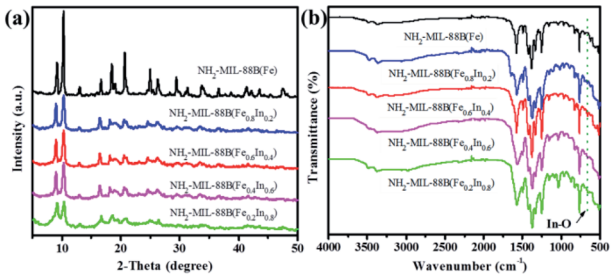

Fig. 1 (a) XRD patterns and (b) FT-IR of NH_2-MIL-88B (Fe) and NH_2-MIL-88B ($Fe_\alpha In_{1-\alpha}$) samples.

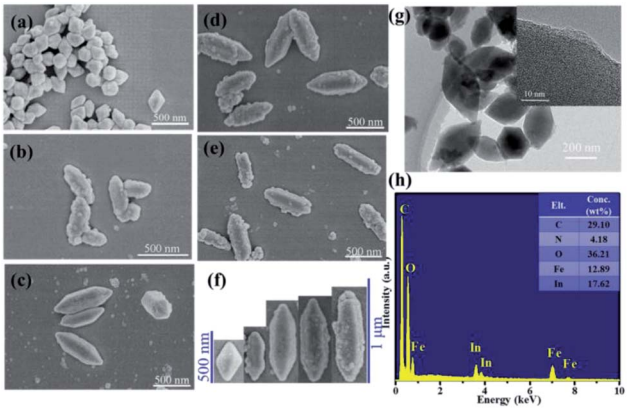

Fig. 2 SEM images of (a) NH_2-MIL-88B (Fe), (b–e) NH_2-MIL-88B ($Fe_\alpha In_{1-\alpha}$) samples (α = 0.8, 0.6, 0.4, 0.2, respectively), (f) the compared SEM images of NH_2-MIL-88B ($Fe_\alpha In_{1-\alpha}$), (g) TEM image of NH_2-MIL-88B ($Fe_{0.6}In_{0.4}$) and (h) EDX image of NH_2-MIL-88B ($Fe_\alpha In_{1-\alpha}$).

of NH_2-MIL-88B (Fe). As the molar ratio of In(III) ions increases, the characteristic peak at 9.21° shifts to 9.02°. The deviation of the characteristic peak might be due to that the ion size of In(III) (94.0 pm) in the crystal structure was significantly larger than the ion size of Fe(III) (78.5 pm), thereby the size of the trimer composed of InO_6 octahedron was larger than that of FeO_6 octahedron in the crystal structure of NH_2-MIL-88B ($Fe_\alpha In_{1-\alpha}$). Therefore, the peak corresponding to the characteristic peak in the spectrum could shift to a lower angle due to the increase of the unit cell parameters.[51]

To further determine the chemical structure and investigate the doped of In(III) of the prepared samples, the FT-IR spectrum is employed to analyze. As presented in Fig. 1b, the FT-IR spectrum of NH_2-MIL-88B (Fe) is consistent with the previous literature.[52] By comparison, after indium doping, a new characteristic absorption peak generation, which could be attributed to the In–O bond appears at 663 cm^{-1}, indicating that In(III) is successfully introduced and the In–O bond is formed. Except for the appearance of new characteristic absorption peaks, the characteristic absorption peaks corresponding to other chemical bonds have not been changed, indicating that the introduction of In(III) does not affect the chemical structure of NH_2-MIL-88B (Fe), NH_2-MIL-88B ($Fe_\alpha In_{1-\alpha}$) was successfully prepared.

Fig. 2a–f displays representative SEM images and length comparison of NH_2-MIL-88B (Fe) and In-doped NH_2-MIL-88B ($Fe_\alpha In_{1-\alpha}$). As shown in Fig. 2a, NH_2-MIL-88B (Fe) performed a standard spindle with uniform morphology, in which the length is 300–500 nm. Additionally, the spindle is continuously elongated in the longitudinal direction with the increase of In(III) ion content as shown in Fig. 2b–f. However, the overall morphology of NH_2-MIL-88B ($Fe_\alpha In_{1-\alpha}$) is unchanged, forming a six-sided double pyramid with a length in the range of 500–1000 nm. The cause of the morphological change may be ascribed to In(III) ions replacing Fe(III) into the NH_2-MIL-88B (Fe) lattice, which increases the lattice spacing in the crystal.[51] The BET specific surface area test results showed that the BET specific surface areas of NH_2-MIL-88B ($Fe_{0.6}In_{0.4}$) is 204 $m^2\ g^{-1}$ less than that of NH_2-MIL-88B (Fe), as Table S2† in details. The pore structure of NH_2-MIL-88B (Fe) was narrowed after the introduction and the specific surface area was relatively reduced because of the large ion size of In(III).

The morphology of the NH_2-MIL-88B ($Fe_{0.6}In_{0.4}$) in the TEM image is a hexagonal prism with sharp ends, as shown in Fig. 2g, which is the same as the result obtained in the SEM image. HRTEM displayed that NH_2-MIL-88B ($Fe_{0.6}In_{0.4}$) has an ordered pore structure, where is difficult to find nanoparticles or metal oxide clusters outside the catalyst. Thence, In(III) has been incorporated into the framework of NH_2-MIL-88B (Fe) instead of being supported on the surface. As shown in Fig. 2h, In and Fe elements were approved in the EDX images, which even demonstrated the conformation of MM-MOFs NH_2-MIL-88B ($Fe_\alpha In_{1-\alpha}$).

XPS analysis

The XPS spectra of NH_2-MIL-88B ($Fe_{0.6}In_{0.4}$) composite is shown in Fig. 3a. There are five characteristic peaks in the survey spectrum, which corresponding to the C 1s, N 1s, In 3d, O 1s, and Fe 2p electron orbitals, respectively. These elements confirm the results of the EDX analysis as displayed in Table S3.† Fig. 3b is the characteristic peak of C, all of them are derived from organic ligands. The characteristic peaks at 284.4, 286.2, and 288.2 eV could be attributed to C=C, C–N and C=O respectively, which correspond to various carbon-containing covalent bonds in NH_2-BDC.[53] In Fig. 3c, the XPS spectrum of N 1s can be divided to 396.8 and 397.9 eV, which represents the $-N=^+$ and $-NH-^+$ respectively. It belonged to the amino group extending or protruding into the cavity and the positively charged. There are four characteristic peaks in the XPS spectrum of O 1s shown in Fig. 3d. The peaks at 531.7 and 530.8 eV can be attributed to –OH and C=O of the organic ligand. Also, 529.9 and 529.1 eV correspond to the characteristic peaks of In–O and Fe–O respectively. The appearance of In–O clusters shows that In(III) has been doped into the catalyst and connected to the organic ligands, thus successfully constructing NH_2-MIL-88B ($Fe_\alpha In_{1-\alpha}$), which is consistent with the results of TEM. Fig. 3e shows the characteristic peaks of Fe 2p, where the satellite peak of Fe is at 715.2 eV. Among the peaks of Fe $2p_{1/2}$ and Fe $2p_{3/2}$, 724.0 eV and 710.0 eV represent Fe^{3+}, and 722.2 eV and 709.0 eV represent Fe^{2+}.[54–56] The appearance of Fe^{2+} is due

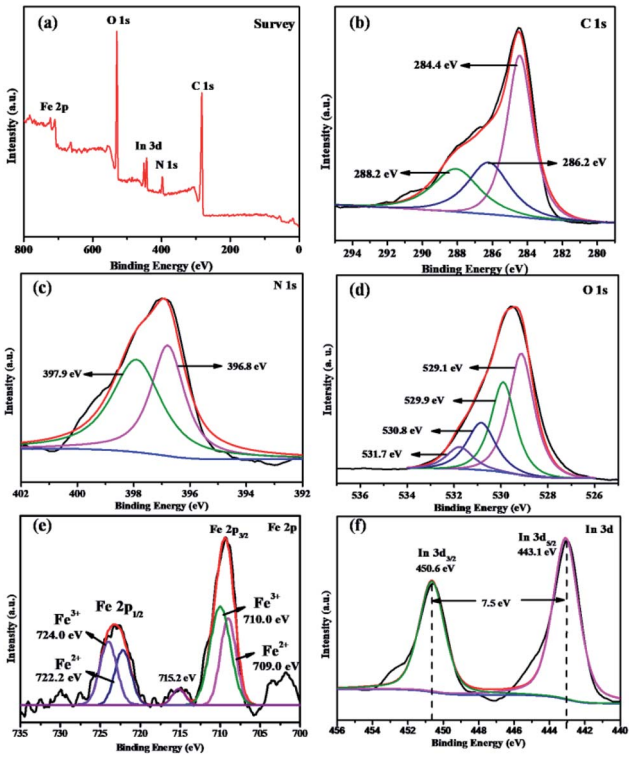

Fig. 3 XPS spectra of NH_2-MIL-88B ($Fe_{0.6}In_{0.4}$) composite (a). Survey; (b) C 1s; (c) N 1s; (d) O 1s; (e) Fe 2p; (f) In 3d, respectively.

to the combination of photogenerated electrons and Fe^{3+}, reducing Fe^{3+} to Fe^{2+}. The peak at 450.6 and 443.1 eV can be verified to In $3d_{3/2}$ and In $3d_{5/2}$ as presented in Fig. 3f, respectively. This once again proves that In is successfully doped in NH_2-MIL-88B ($Fe_\alpha In_{1-\alpha}$). Contacted with the characterization results of XRD, IR, EDS, and XPS, it can be further confirmed that the In-doped NH_2-MIL-88B ($Fe_\alpha In_{1-\alpha}$) bimetallic material has been successfully prepared.

Optical properties

The UV-vis DRS spectra of the samples were used to demonstrate the optical absorption properties in Fig. 4a. As reduced, the absorption intensity of NH_2-MIL-88B ($Fe_\alpha In_{1-\alpha}$) gradually decreases in the visible light region. NH_2-MIL-88B ($Fe_{0.8}In_{0.2}$) has the strongest absorption intensity of visible light, and NH_2-MIL-88B ($Fe_{0.6}In_{0.4}$) has a slight enhance in visible light absorption intensity. Comparing with NH_2-MIL-88B (Fe), both have significantly enhanced visible light absorption. Thereby, this indicates that a certain proportion of In(III) doping, which is beneficial to improve the visible light absorption capacity of NH_2-MIL-88B (Fe).

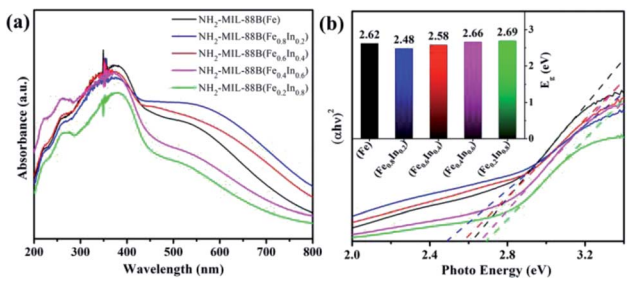

Fig. 4 (a) UV-vis DRS spectrum and (b) plots of $(\alpha h\nu)^2$ *versus* photon energy ($h\nu$) of the NH_2-MIL-88B (Fe) and the NH_2-MIL-88B ($Fe_\alpha In_{1-\alpha}$) samples.

The corresponding bandgap energy (E_g) values could be calculated by following the eqn (1)

$$(\alpha h\nu)^2 = A(h\nu - E_g) \quad (2)$$

here, α, h, ν, A, E_g corresponds to the absorption coefficient, the Planck's constant, light frequency, constant, the bandgap energy, respectively. As displayed in Fig. 4b, the E_g values of NH_2-MIL-88B (Fe), NH_2-MIL-88B ($Fe_{0.8}In_{0.2}$), NH_2-MIL-88B ($Fe_{0.6}In_{0.4}$), NH_2-MIL-88B ($Fe_{0.4}In_{0.6}$) and NH_2-MIL-88B ($Fe_{0.2}In_{0.8}$) were estimated to be 2.62, 2.48, 2.58, 2.66 and 2.69 eV, respectively. The size of the bandgap energy is related to the difficulty of electronic excitation. Under visible light irradiation, the lower bandgap energy can allow more electrons to excite the transition to CB, promote the effective separation of electrons and holes, thereby improving the photocatalytic activity. Among them, NH_2-MIL-88B ($Fe_{0.8}In_{0.2}$) and NH_2-MIL-88B ($Fe_{0.6}In_{0.4}$) displayed the lower E_g and the stronger visible light response-ability, which may perform better photocatalytic performance.

As shown in Fig. S1,† the fluorescence intensity of NH_2-MIL-88B ($Fe_{0.6}In_{0.4}$) is significantly lower than that of NH_2-MIL-88B (Fe), which indicates that the addition of In(III) inhibits the recombination of photogenerated e^-–h^+, thereby allowing more photogenerated carriers to participate photocatalytic reaction.[57,58]

Photocatalytic activities

For verifying the photocatalytic performance of NH_2-MIL-88B ($Fe_\alpha In_{1-\alpha}$) obtained from the characterization results, we conducted experiments on photocatalytic Cr(VI) reduction under different catalytic conditions. As displayed in Fig. 5a, the Cr(VI) concentration was unaltered significantly with visible light irradiation and no photocatalyst, at the same time, the small range change of Cr(VI) concentration was due to adsorption with photocatalyst and no light, which indicated that visible light irradiation played an important role in the photocatalytic reduction of Cr(VI). The photocatalytic reduction efficiency of NH_2-MIL-88B ($Fe_{0.6}In_{0.4}$) for reducing Cr(VI) is 86.83%, which is significantly higher 1.7 times than that of NH_2-MIL-88B (Fe) of 50.96%, thereby, which demonstrated that the doping of In(III) effectively improves the photocatalytic reduction performance. As shown in Fig. 5b, the different In(III) doped amount of NH_2-MIL-88B ($Fe_\alpha In_{1-\alpha}$) was carried out to discuss the capability of photocatalytic Cr(VI) reduction. With the doping of In, the photocatalytic reduction effect of the catalyst gradually increases. Among them, NH_2-MIL-88B ($Fe_{0.6}In_{0.4}$) has the highest photocatalytic reduction rate. By contrast, NH_2-MIL-88B ($Fe_{0.8}In_{0.2}$) is the lowest one. With the addition of more In(III) content, the catalytic effect gradually decreases. This may be due to more In(III) doping, resulting in lower visible light absorption. And higher bandgap energy is not conducive to the

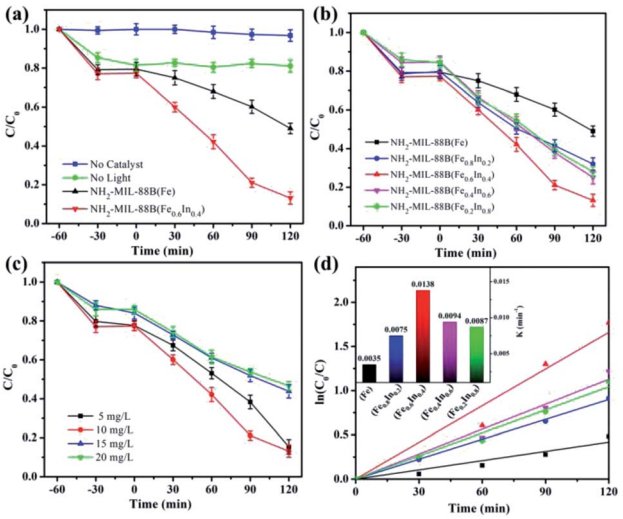

Fig. 5 Photocatalytic reduction of Cr(VI) (a) blank group comparison, (b) NH_2-MIL-88B ($Fe_\alpha In_{1-\alpha}$), (c) Cr(VI) on different concentrations reduction performance, and (d) the fitting of the pseudo-first-order linear line for the photocatalytic reaction. (Reaction conditions: 0.5 g L^{-1} photocatalyst, 3 mL ethanol, RT, pH = 2).

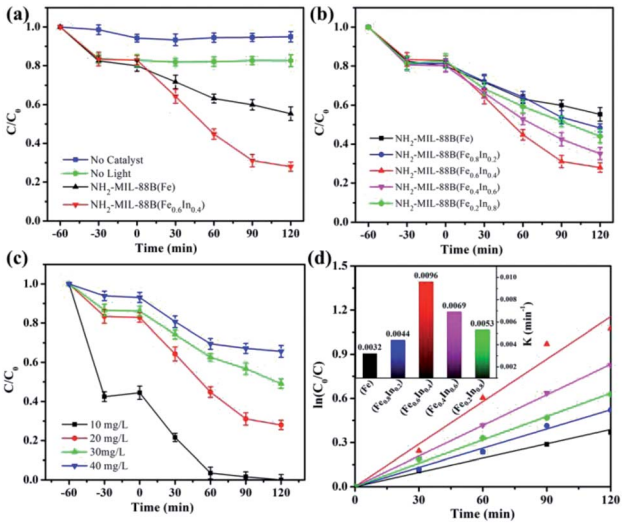

Fig. 6 Photocatalytic degradation of TC-HCl (a) blank group comparison, (b) NH_2-MIL-88B ($Fe_\alpha In_{1-\alpha}$), (c) TC-HCl on different concentrations degradation performance and (d) the fitting of the pseudo-first-order linear line for the photocatalytic reaction. (Reaction conditions: 0.1 g L^{-1} photocatalyst, RT).

excitation of electrons on VB, thereby reducing the photocatalytic activity of photocatalytic reduction of hexavalent chromium. Meanwhile, Fig. 5c shows that the photocatalytic Cr(VI) on different concentrations reduction performance of NH_2-MIL-88B ($Fe_{0.6}In_{0.4}$) was investigated. With increasing the amount of catalyst, the photocatalytic performance gradually increases, reaching the maximum at 10 mg L^{-1}. However, an excess of the catalyst leads to lower photocatalytic reduction efficiency. This may be due to excessive catalyst hindering the light irradiation of the Cr(VI) solution. Fig. 5d displays that the photocatalytic reduction efficiency has a good linear relationship with the reaction time, which conforms to the first-order reaction kinetics. The pseudo-first-order rate constant k is obtained by the following formula:

$$\ln(C_0/C) = kt \quad (3)$$

here, C_0, C, k, and t corresponds to the initial concentrations of Cr(VI), the concentrations of Cr(VI), the pseudo-first-order rate constant, and time, respectively. The value of k and R^2 of NH_2-MIL-88B (Fe) and NH_2-MIL-88B ($Fe_\alpha In_{1-\alpha}$) was displayed in Tables S4 and S5.†

To investigate the oxidation performance of the prepared photocatalyst, the photocatalytic degradation of TC-HCl by NH_2-MIL-88B ($Fe_\alpha In_{1-\alpha}$) under different catalytic conditions was performed. Similar to the photocatalytic reduction effect of Cr(VI), the test result of Fig. 6a shows that the light and photocatalyst are crucial in the reaction system. As shown in Fig. 6b, the photocatalytic degradation efficiency of NH_2-MIL-88B ($Fe_{0.6}In_{0.4}$) on TC-HCl under visible light irradiation conditions is 72.05%, which is significantly higher 1.6 times than that of NH_2-MIL-88B (Fe) of 44.68%. Fig. 6c demonstrated the effect of different concentrations photocatalytic degradation efficiency of TC-HCl. Among them, as the content of TC-HCl increases, the degradation rate gradually decreases, and when the content is 10 mg, NH_2-MIL-88B ($Fe_{0.6}In_{0.4}$) displays the best degradation effect. The relationship between $\ln(C_0/C)$ and time shows that the photocatalytic degradation efficiency has a good linear relationship with the reaction time, as presented in Fig. 6d, which is in line with the first-order reaction kinetics. The value of k and R^2 of NH_2-MIL-88B (Fe) and NH_2-MIL-88B ($Fe_\alpha In_{1-\alpha}$) was displayed in Tables S6 and S7.†

To detect the reactive oxygen species generation during the photocatalytic degradation of TC-HCl by NH_2-MIL-88B ($Fe_\alpha In_{1-\alpha}$), electron spin resonance (ESR) technique is employed. Fig. 7 depicts the conspicuous characteristic peak signals of DMPO-$^{\bullet}O_2^-$ and DMPO-$^{\bullet}$OH, which confirms the generation of $^{\bullet}O_2^-$ and $^{\bullet}$OH radicals in the experiment. The peak intensity ratio of the quadruple characteristic peak signal of DMPO-$^{\bullet}$OH is about 1 : 2 : 2 : 1.[59] NH_2-MIL-88B ($Fe_\alpha In_{1-\alpha}$) by the photoexcitation generates e^- under visible light irradiation, which can activate dissolved oxygen in the solution that promotes oxygen molecules to become $^{\bullet}O_2^-$ species and can

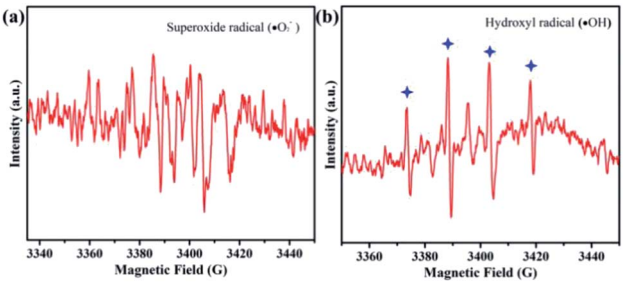

Fig. 7 ESR spectra of DMPO-$^{\bullet}O_2^-$ and DMPO-$^{\bullet}$OH adducts generated NH_2-MIL-88B ($Fe_\alpha In_{1-\alpha}$) after 60 seconds under visible light irradiation (λ > 400 nm) during the photocatalytic process.

also interact with water molecules to generate $^{\bullet}OH$ species, simultaneously.

Mechanism

Based on the above results, the possible mechanism of NH_2-MIL-88B ($Fe_\alpha In_{1-\alpha}$) photocatalytic treatment of Cr(VI) and TC-HCl in water is proposed. First, the electrons transfer process of NH_2-MIL-88B ($Fe_\alpha In_{1-\alpha}$) photocatalytic reduction of Cr(VI) is as follows. Under visible light irradiation, the organic ligand of NH_2-MIL-88B ($Fe_\alpha In_{1-\alpha}$) can be excited to generate electrons and holes. A part of the photogenerated electrons transfers to the surface of the catalyst through the In–O clusters through the LMCT to reduce Cr(VI) adsorbed directly. Then, the In–O clusters transfer another electron to the Fe–O cluster through MMCT, which promotes the separation of electrons and holes effectively.[49] The excitation and transfer of photogenerated carriers of photocatalytic oxidation of TC-HCl are similar to the process of reduction of Cr(VI). The photogenerated electrons transfer to the surface of the catalyst combine with O_2 and H_2O in the solution to produce $^{\bullet}O_2^-$ and $^{\bullet}OH$. Both the holes generated by NH_2-MIL-88B ($Fe_\alpha In_{1-\alpha}$) excited by visible light and $^{\bullet}O_2^-$/$^{\bullet}OH$ can interact with TC-HCl directly and eventually generate to CO_2 and H_2O. Anyway, the MMCT in the NH_2-MIL-88B ($Fe_\alpha In_{1-\alpha}$) expands the active sites of photocatalytic oxidation-reduction. Also, the synergistic process of LMCT and MMCT effectively inhibits the recombination of electrons and holes, thereby enhancing the performance of the NH_2-MIL-88B ($Fe_\alpha In_{1-\alpha}$) (Scheme 2).

Conclusions

In summary, a series of NH_2-MIL-88B ($Fe_\alpha In_{1-\alpha}$) photocatalysts were designed and synthesized *via* a one-pot method. Proved by characterizations of TEM and XPS, In(III) ions successfully replaced part of Fe(III) ions in the structure, which formed mixed-metal MOFs NH_2-MIL-88B ($Fe_\alpha In_{1-\alpha}$). Compared with single NH_2-MIL-88B (Fe), NH_2-MIL-88B ($Fe_{0.6}In_{0.4}$) shows excellent photocatalytic performance: the reduction rate of Cr(VI) and the oxidation rate of TC-HCl reach 86.83% and 72.05%, which 1.7 and 1.6 times that of NH_2-MIL-88B (Fe), respectively. The improvement of photocatalytic performance is mainly attributed to the more reactive sites when In(III) doped to NH_2-MIL-88B (Fe). Simultaneously, the synergistic effect of LMCT and MMCT of NH_2-MIL-88B ($Fe_\alpha In_{1-\alpha}$) effectively expands the separation and transfer of photogenerated carriers and inhibits the recombination of electrons–holes pairs, thereby enhancing the performance of photocatalytic reduction of Cr(VI) and oxidative degradation of TC-HCl. This work may provide an insight to design and develop mixed-metal MOFs as photocatalysts for the wastewater treatment.

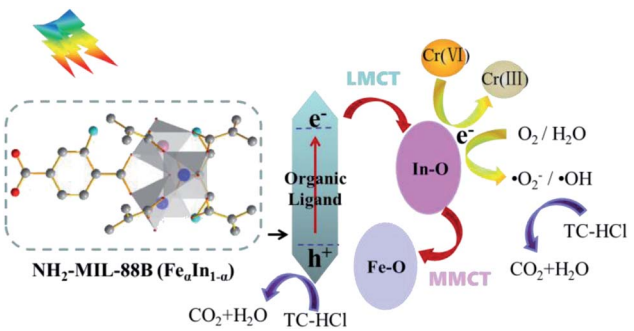

Scheme 2 Possible mechanism of photocatalytic degradation of Cr(VI) and TC-HCl by NH_2-MIL-88B ($Fe_\alpha In_{1-\alpha}$).

Conflicts of interest

There are no conflicts to declare.

Acknowledgements

Thanks to the 2020 School-level Scientific Research Project of Dalian Vocational & Technical College (Dalian Radio and TV University) and the Key Project of Natural Science Foundation of Liaoning Province (No. 20170540578).

References

1 X. H. Yi, F. X. Wang, X. D. Du, H. Fu and C. C. Wang, *Polyhedron*, 2018, **152**, 216–224.
2 H. Xie, J. Zhang, D. Wang, J. Liu, L. Wang and H. Xiao, *Appl. Surf. Sci.*, 2020, **504**, 144456.
3 L. Zeng, X. Li, S. Fan, M. Zhang, Z. Yin, M. Tadé and S. Liu, *ACS Appl. Energy Mater.*, 2018, **1**, 3752–3762.
4 L. Zeng, X. Li, S. Fan, Z. Yin, J. Mu, M. Qin and A. Chen, *J. Power Sources*, 2020, **478**, 228755.
5 F. Yuan, Z. Sun, C. Li, Y. Tan, X. Zhang and S. Zheng, *J. Hazard. Mater.*, 2020, **396**, 122694.
6 D. D. Chen, X. H. Yi, C. Zhao, H. Fu, P. Wang and C. C. Wang, *Chemosphere*, 2020, **245**, 125659.
7 S. Wu, Y. Ge, Y. Wang, X. Chen, F. Li, H. Xuan and X. Li, *Environ. Technol.*, 2017, **39**, 1937–1948.
8 F. Wei, D. Chen, Z. Liang, S. Zhao and Y. Luo, *Dalton Trans.*, 2017, **46**, 16525–16531.
9 C. Peng, H. Meng, S. Song, S. Lu and A. Lopez-Valdivieso, *Sep. Sci. Technol.*, 2005, **39**, 1501–1517.
10 R. K. Goyal, N. S. Jayakumar and M. A. Hashim, *J. Hazard. Mater.*, 2011, **195**, 383–390.
11 R. K. Misra, S. K. Jain and P. K. Khatri, *J. Hazard. Mater.*, 2011, **185**, 1508–1512.
12 Y. J. Zhang, J. L. Ou, Z. K. Duan, Z. J. Xing and Y. Wang, *Colloids Surf., A*, 2015, **481**, 108–116.
13 L. Shi, T. Wang, H. Zhang, K. Chang, X. Meng, H. Liu and J. Ye, *Adv. Sci.*, 2015, **2**, 1500006.
14 R. Liang, F. Jing, L. Shen, N. Qin and L. Wu, *J. Hazard. Mater.*, 2015, **287**, 364–372.
15 L. Zeng, X. Li, S. Fan, M. Zhang, Z. Yin, M. Tadé and S. Liu, *J. Power Sources*, 2019, **413**, 310–317.
16 C. Zhao, Z. Wang, X. Li, X. Yi, H. Chu, X. Chen and C. C. Wang, *Chem. Eng. J.*, 2020, **389**, 123431.
17 H. Xie, D. Ma, W. Liu, Q. Chen, Y. Zhang, J. Huang, H. Zhang, Z. Jin, T. Luo and F. Peng, *New J. Chem.*, 2020, **44**, 7218–7225.

18 J. Ke, H. Zhou, J. Liu, Z. Zhang, X. Duan and S. Wang, *J. Colloid Interface Sci.*, 2019, **555**, 413–422.
19 H. Fakhri and H. Bagheri, *Mater. Sci. Semicond. Process.*, 2020, **107**, 104815.
20 D. Wang, F. Jia, H. Wang, F. Chen, Y. Fang, W. Dong, G. Zeng, X. Li, Q. Yang and X. Yuan, *J. Colloid Interface Sci.*, 2018, **519**, 273–284.
21 Y. Zhang, J. Zhou, X. Chen, L. Wang and W. Cai, *Chem. Eng. J.*, 2019, **369**, 745–757.
22 L. L. Yu, W. Cao, S. C. Wu, C. Yang and J. H. Cheng, *Ecotoxicol. Environ. Saf.*, 2018, **164**, 289–296.
23 X. Wen, Y. Jia and J. Li, *J. Hazard. Mater.*, 2010, **177**, 924–928.
24 T. Chen, R. Tsai, Y. Chen and K. Huang, *Int. J. Electrochem. Sci.*, 2014, **9**, 8422–8434.
25 K. Kosutic, D. Dolar, D. Asperger and B. Kunst, *Sep. Purif. Technol.*, 2007, **53**, 244–249.
26 K. J. Choi, H. J. Son and S. H. Kim, *Sci. Total Environ.*, 2007, **387**, 247–256.
27 Y. Gao, J. Wu, J. Wang, Y. Fan, S. Zhang and W. Dai, *ACS Appl. Mater. Interfaces*, 2020, **12**, 11036–11044.
28 J. Ke, C. Zhao, H. Zhou, X. Duan and S. Wang, *Sustainable Mater. Technol.*, 2019, **19**, e00088.
29 J. Liu, J. Zhang, D. Wang, D. Li, J. Ke, S. Wang, S. Liu, H. Xiao and R. Wang, *ACS Sustainable Chem. Eng.*, 2019, **7**, 12428–12438.
30 J. Li, X. Li, L. Zeng, S. Fan, M. Zhang, W. Sun, X. Chen, M. O. Tade and S. Liu, *Nanoscale*, 2019, **11**, 3877–3887.
31 S. Y. Fan, X. Y. Li, Q. D. Zhao, L. B. Zeng, M. M. Zhang, Z. F. Yin, T. T. Lian, M. O. Tad and S. M. Liu, *Dalton Trans.*, 2018, **47**, 12769–12782.
32 Y. P. Zhu, J. Yin, E. Abou-Hamad, X. Liu, W. Chen, T. Yao, O. F. Mohammed and H. N. Alshareef, *Adv. Mater.*, 2020, **32**, e1906368.
33 C. V. Reddy, K. R. Reddy, V. V. N. Harish, J. Shim, M. V. Shankar, N. P. Shetti and T. M. Aminabhavi, *Int. J. Hydrogen Energy*, 2020, **45**, 7656–7679.
34 J. Wang, X. Liu, C. Li, M. Yuan, B. Zhang, J. Zhu and Y. Ma, *J. Photochem. Photobiol., A*, 2020, **401**, 112795.
35 L. Zeng, X. Li, S. Chen, J. Wen, W. Huang and A. Chen, *J. Mater. Chem. A*, 2020, **8**, 7339–7349.
36 S. Zhang, M. Du, Z. Xing, Z. Li, K. Pan and W. Zhou, *Appl. Catal., B*, 2020, **262**, 118202.
37 J. Ye, J. Liu, Z. Huang, S. Wu, X. Dai, L. Zhang and L. Cui, *Chemosphere*, 2019, **227**, 505–513.
38 Z. H. Yang, J. Cao, Y. P. Chen, X. Li, W. P. Xiong, Y. Y. Zhou, C. Y. Zhou, R. Xu and Y. R. Zhang, *Microporous Mesoporous Mater.*, 2019, **277**, 277–285.
39 M. A. Nasalevich, M. van der Veen, F. Kapteijn and J. Gascon, *CrystEngComm*, 2014, **16**, 4919–4926.
40 J. Liu and Y. Pan, *Metal-Organic Frameworks for Biomedical Applications*, 2020, pp. 45–68, DOI: 10.1016/b978-0-12-816984-1.00004-4.
41 A. Beziau, S. A. Baudron, A. Fluck and M. W. Hosseini, *Inorg. Chem.*, 2013, **52**, 14439–14448.
42 W. S. El-Yazeed, Y. G. El-Reash, L. A. Elatwy and A. I. Ahmed, *RSC Adv.*, 2020, **10**, 9693–9703.
43 M. Y. Masoomi, A. Morsali, A. Dhakshinamoorthy and H. Garcia, *Angew. Chem.*, 2019, **58**, 15188–15205.
44 M. R. D. Khaki, M. S. Shafeeyan, A. A. A. Raman and W. Daud, *J. Environ. Manage.*, 2017, **198**, 78–94.
45 D. Ge, G. Qu, X. Li, K. Geng, X. Cao and H. Gu, *New J. Chem.*, 2016, **40**, 5531–5536.
46 W. Zhang, Y. Shi, C. Li, Q. Zhao and X. Li, *Catal. Lett.*, 2016, **146**, 1956–1964.
47 T. A. Vu, G. H. Le, C. D. Dao, L. Q. Dang, K. T. Nguyen, P. T. Dang, H. T. K. Tran, Q. T. Duong, T. V. Nguyen and G. D. Lee, *RSC Adv.*, 2014, **4**, 41185–41194.
48 M. Perfecto-Irigaray, J. Albo, G. Beobide, O. Castillo, A. Irabien and S. Pérez-Yáñez, *RSC Adv.*, 2018, **8**, 21092–21099.
49 S. Wang, F. Meng, X. Sun, M. Bao, J. Ren, S. Yu, Z. Zhang, J. Ke and L. Zeng, *Appl. Surf. Sci.*, 2020, **528**, 147053.
50 L. Wang, S. Duan, M. Fang, J. Liu, J. He, J. Li and J. Lei, *RSC Adv.*, 2016, **6**, 71250–71261.
51 S. A. Park, H. J. Lee, Y. J. Cho, S. Choi and M. Oh, *Chem. – Eur. J.*, 2014, **20**, 5559–5564.
52 A. Samui, A. R. Chowdhuri, T. K. Mahto and S. K. Sahu, *RSC Adv.*, 2016, **6**, 66385–66393.
53 Z. D. Lei, Y. C. Xue, W. Q. Chen, L. Li, W. H. Qiu, Y. Zhang and L. Tang, *Small*, 2018, **14**, e1802045.
54 H. Y. Zhang, L. Wang, C. F. Guo, J. Q. Ning, Y. J. Zhong and Y. Hu, *ChemNanoMat*, 2020, **6**, 1325–1331.
55 H. Liu, K. Tian, J. Ning, Y. Zhong, Z. Zhang and Y. Hu, *ACS Catal.*, 2019, **9**, 1211–1219.
56 H. Zhang, C. Guo, J. Ren, J. Ning, Y. Zhong, Z. Zhang and Y. Hu, *Chem. Commun.*, 2019, **55**, 14050–14053.
57 L. Li, C. Guo, J. Shen, J. Ning, Y. Zhong and Y. Hu, *Chem. Eng. J.*, 2020, **400**, 125925.
58 H. Liu, L. Li, C. Guo, J. Ning, Y. Zhong and Y. Hu, *Chem. Eng. J.*, 2020, **385**, 123929.
59 X. Li, Y. Pi, L. Wu, Q. Xia, J. Wu, Z. Li and J. Xiao, *Appl. Catal., B*, 2017, **202**, 653–663.

